Electronic Supplementary Material (ESI) for Energy & Environmental Science.
This journal is © The Royal Society of Chemistry 2021

Supplementary Information

Highly Efficient Transverse Thermoelectric Devices with Re_4Si_7 Crystals

Michael R. Scudder[a], Bin He[b], Yaxian Wang[c], Akash Rai[d], David G. Cahill[d], Wolfgang Windl[c], Joseph P. Heremans[b,c,e], Joshua E. Goldberger[a]

[a]Department of Chemistry and Biochemistry, The Ohio State University, Columbus, OH 43210

[b]Department of Mechanical and Aerospace Engineering, The Ohio State University, Columbus, OH 43210

[c]Department of Materials Science and Engineering, The Ohio State University, Columbus, OH 43210

[d]Department of Materials Science and Engineering and Materials Research Laboratory, University of Illinois at Urbana-Champaign, Urbana, Illinois 61801, USA

[e]Department of Physics, The Ohio State University, Columbus, OH 43210

Supplement S1. Estimate of the efficiency loss in conventional thermoelectric modules

In the main text, it is claimed that modules lose an additional 30 to 50 % of the thermoelectric efficiency over the zT of the thermoelectric material. This figure is arrived at as follows. The effective module ZT can be estimated from the modules specified maximum temperature drop in refrigeration mode ΔT_M by the formula $\Delta T_M = (ZT/2)\ T_C$.[1] ΔT_M =72K is typical for modules that operate between 280 and 350 K: this gives ZT=0.52. The maximum zT of commercial semiconductor elements typically used in such modules is 0.95 for *n*-type material and 1.1 for *p*–type material but averages to 0.85 for *n*-type and 0.95 for *p*-type material[2] over the 280-350K temperature range, for a 42% loss between material zT and module ZT. It should be pointed out that the module ZT can be adjusted by the manufacturers by simply cutting the semiconductor elements shorter or longer, thereby altering the relative effect of the contact resistances compared to the element resistance but also altering the materials cost. This variation is the basis for the 30-50% bracket cited in the main text.

Supplement S2: Transverse Thermopower and $z_{xy}T$ in terms of IP and CP materials properties

The transverse thermopower α_{xy} (see **Fig. 1c**) is derived from the thermopowers along the in-plane (α_{IP}) and cross-plane (α_{CP}) directions, by rotating the coordinate system from the (*x,y*) axes to the (*IP, CP*) axes using a rotation tensor.[3] The thermopower tensor along the high-symmetry directions (*IP, CP*) of the crystal, has bloy hypothesis no off-diagonal components: the electric fields remains parallel to the temperature gradient along both *IP* and *CP* directions, albeit with a different ratio depending on whether the direction is *IP* or *CP*:

$$\overleftrightarrow{\alpha} = \begin{bmatrix} \alpha_{IP} & 0 \\ 0 & \alpha_{CP} \end{bmatrix} \tag{S2.1}$$

Since *x* and *y* are not necessarily high-symmetry axes of the crystal, however, the thermopower tensor in the (*x,y*) system can have off-diagonal components, and in general looks like

$$\overleftrightarrow{\alpha}' = \begin{bmatrix} \alpha_{xx} & \alpha_{xy} \\ \alpha_{yx} & \alpha_{yy} \end{bmatrix} \tag{S2.2}$$

If the (*x,y*) and the (*IP, CP*) axes are both normal but rotated by an angle θ with respect to each other, one can transform one tensor into the other by applying a rotation tensor $\overleftrightarrow{R}$ as $\overleftrightarrow{\alpha}' = \overleftrightarrow{R}\,\overleftrightarrow{\alpha}\,\overleftrightarrow{R}^T$:

$$\begin{bmatrix} \alpha_{xx} & \alpha_{xy} \\ \alpha_{yx} & \alpha_{yy} \end{bmatrix} = \begin{bmatrix} cos(\theta) & -sin(\theta) \\ sin(\theta) & cos(\theta) \end{bmatrix} \begin{bmatrix} \alpha_{IP} & 0 \\ 0 & \alpha_{CP} \end{bmatrix} \begin{bmatrix} cos(\theta) & -sin(\theta) \\ sin(\theta) & cos(\theta) \end{bmatrix}^{-1} \tag{S2.3}$$

from which Eq. (2) follows immediately. α_{xy} is maximized for θ=45°, in a material in which α_{IP} and α_{CP} are of opposite polarity, and $|\alpha_{IP}|$ and $|\alpha_{CP}|$ are as large as possible. Zhou et al[4] derived the thermal conductivity, electrical resistivity and $z_{xy}T$ expressed in the (*x,y*) coordinate system in terms of their equivalent in the (*IP,CP*) system: electrical resistivities ρ_{IP}, ρ_{CP} and thermal conductivities κ_{IP}, κ_{CP}. They also calculated the angle θ_{OPT} for which the $z_{xy}T$ is maximized, which is different from the value that maximizes α_{xy} :

$$cos^2\theta_{OPT} = \left(1 + \sqrt{\frac{\kappa_{CP}/\kappa_{IP}}{\rho_{CP}/\rho_{IP}}}\right)^{-1} \tag{S2.4}$$

For Re_4Si_7, $\theta_{OPT} \sim 52°$ at 980 K, and changes slightly at different temperatures. With this value of the angle, the $z_{xy}T$ now becomes:

$$z_{xy}T = \frac{(\alpha_{IP}-\alpha_{CP})^2 T}{\left(\sqrt{\kappa_{CP}\rho_{CP}}+\sqrt{\kappa_{IP}\rho_{IP}}\right)^2} \tag{S2.5}$$

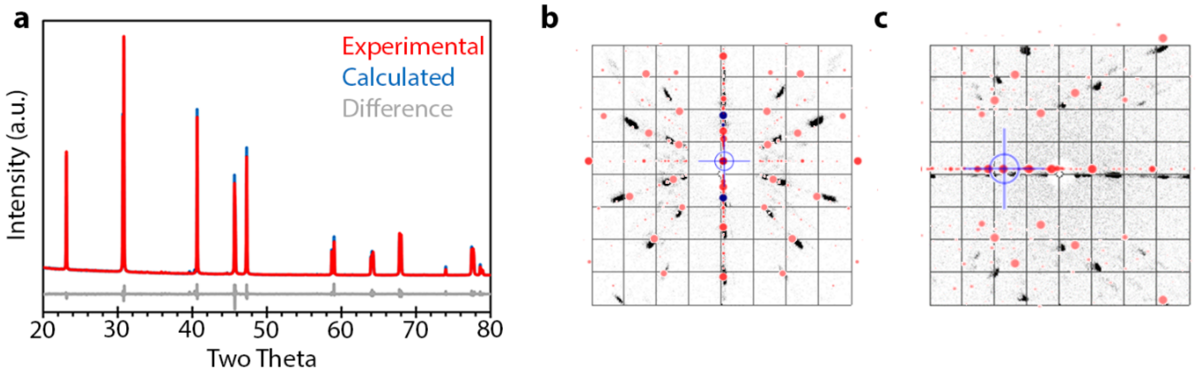

Figure S1: **Material characterization**. **a**, PXRD of Re_4Si_7 crystal used for study. **b**, Laue diffraction pattern for *a* [100] face, Re_4Si_7. **c**, Laue diffraction pattern for *c*[001] edge, Re_4Si_7. For **b** and **c** experimental Laue diffraction patterns are in black, predicted Laue patterns are in red.

Supplement S3. Non-monotonic thermopower in intrinsic semiconductors

In practice all semiconductors have a residual non-intentional doping level, which at low temperature pins the chemical potential in either the conduction or the valence bands. Under those circumstances, the partial thermopower is $\boldsymbol{\alpha} = \left(\frac{\boldsymbol{\pi}^2}{\mathbf{2}}\right)\left(\frac{\boldsymbol{k_B}}{\boldsymbol{e}}\right)\left(\frac{\boldsymbol{k_B T}}{\boldsymbol{E_F}}\right)$ (assuming acoustic phonon scattering) and increases with increasing T. If the non-intentional doping level is small enough that above a certain temperature (T_M) both electrons and holes become thermally activated in sufficient numbers as to overwhelm the non-intentional carriers, the semiconductor is called intrinsic. In the presence of both electron and hole carrier types, the total thermopower is given by the conductivity-weighted average of the partial thermopowers:

$$\alpha = (\alpha_e \sigma_e + \alpha_h \sigma_h)(\sigma_e + \sigma_h)^{-1} \tag{S3.1}$$

Since $\alpha_h>0$ and $\alpha_e<0$, the partial thermopowers of electrons and holes compensate each other and

in an intrinsic semiconductor (at $T>T_M$), the total thermopower decreases with increasing T.

The final result for the thermopower of a near-intrinsic semiconductor such as Re_4Si_7 is a curve for $|\alpha(T)|$ that has a maximum near T_M..

A rule of thumb in semiconductor physics is that at all temperatures, the product of the temperature and the thermopower must be smaller than the energy gap E_g, or $|\alpha|T < E_g$. Empirically, it is found that in most conventional semiconductors, $Eg \approx 2|\alpha|T$:

Ge[5]: maximum $|\alpha|T$=0.3 eV, E_g=0.6 eV,

Si[6]: maximum $|\alpha|T$ = 0.5 eV at 450 K, E_g=1 eV,

While the inequality holds more narrowly in narrow-gap materials:

PbTe[7]: Maximum at 600K (10^{19} doped) => $|\alpha|T$=0.18 eV, E_g=0.2 eV,

Bi_2Te_3[8]: Maximum at 400 K (10^{19} doped) => $|\alpha|T$=0.1 eV, E_g= 0.11 eV,

The *CP* thermopower of Re_4Si_7 (**Fig. 2a**) is an exception to the $|\alpha|T < E_g$ rule, but it is not the only one. The narrow-gap semiconductor $Bi_{82}Sb_{18}$,[9] has E_g=0.011 eV, but α_{33}= -100 μV K^{-1} at 300 K giving $|\alpha_{33}|T$ =0.03 eV. Exceptions occur in narrow gap semiconductors with a very large difference between electron and hole mobilities, which decreases the effectiveness of the compensation of the majority carrier thermopower by the minority carriers.

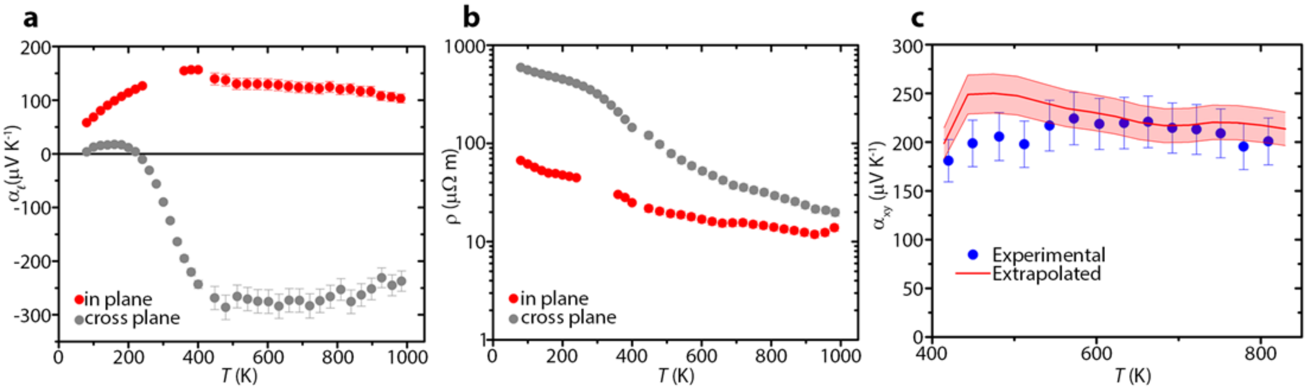

Figure S2: **Thermoelectric data for near intrinsic Re_4Si_7 crystal 2. a,** Temperature-dependent longitudinal thermopower coefficient from 100-980 K. **b,** Temperature-dependent electrical resistivity from 100-980 K. **c,** Transverse thermopower coefficient, 330-900 K.

Supplement S4: Estimation of the Ambipolar Thermal Conductivity

In the main text, we extrapolate the thermal conductivity at high temperature using the Wiedemann-Franz law assuming a Lorenz number (L_0) of 2.44 x 10^{-8} $W\Omega K^{-2}$ and by assuming a constant lattice thermal conductivity.

However, we can also extrapolate the thermal conductivity by considering an ambipolar contribution to the electronic component as well as more precisely modeling the drop in lattice component above the Debye temperature. Here we show that extrapolating the high temperature thermal conductivity using this method leads to a slightly *smaller* thermal conductivity estimate.

Assuming a two-carrier system, the thermal conductivity of Re_4Si_7 at high temperature can potentially contain an ambipolar contribution. Using a formula for ambipolar thermal conductivity from the literature,[10] the Lorenz number for the ambipolar term is given by:

$$L_{ambi} = \frac{b}{(1+b)^2}(|S_e| + |S_h|)^2 \qquad \text{(S4.1)}$$

Where

$$b = \frac{n_e\mu_e}{n_h\mu_h} \qquad \text{(S4.2)}$$

And the ambipolar thermal conductivity is given by

$$\kappa_{ambi} = L_{ambi}\sigma T \qquad \text{(S4.3)}$$

Since our sample of Re_4Si_7 exhibits negligible magnetothermopower and the Hall resistivity is linear in field, the in-plane thermopower is assumed to be dominated by holes and cross-plane thermopower by electrons, so that the in-plane and cross-plane Lorenz number is:

$$\overleftrightarrow{L_{ambi}} = \begin{bmatrix} L_{ip} & 0 \\ 0 & L_{cp} \end{bmatrix} = \begin{bmatrix} \frac{b}{(1+b)^2}S_h^2 & 0 \\ 0 & \frac{b}{(1+b)^2}S_e^2 \end{bmatrix} \qquad \text{(S4.4)}$$

There are still 2 parameters in this formula, which are the carrier density ratio n_e/n_h and the mobility ration m_e/m_h. Assuming a constant scattering time approximation for both electrons and holes (which has been also approximated by Gu *et al.)*[11], the mobility ratio is calculated by the product of effective mass.

$$\mu' = \frac{\mu_e}{\mu_h} = \frac{\tau_e/m^*_e}{\tau_h/m^*_h} \sim \frac{m^*_h}{m^*_e} \qquad \text{(S4.5)}$$

From our DFT calculations (Fig 1F), the effective mass ratios along the cross-plane and in-plane directions are:

Cross-plane:

$$\mu'_{10-1} = \frac{0.26}{7.7} = 0.034$$

In-plane:

$$\mu'_{70-1} = \frac{0.49}{0.1} = 4.9$$

$$\mu'_{010} = \frac{0.87}{0.25} = 3.5$$

Along the in-plane direction, the effective mass ratio is between 3.5 and 4.3 whereas along the out-of-plane direction, the holes have very low mobility.

With different carrier density ratio $n' = n_e / n_h$, the factor *b* and thus the ambipolar Lorenz number L_{ambi} can be calculated. Since we know that the carrier concentration of holes is much higher than that of electrons, here we assume a value of 1 for simplicity. This brings the factor b to be. $b_{ip} = 4.9, b_{cp} = 0.034$. We then plug the values into the ambipolar formula, and the results are shown below;

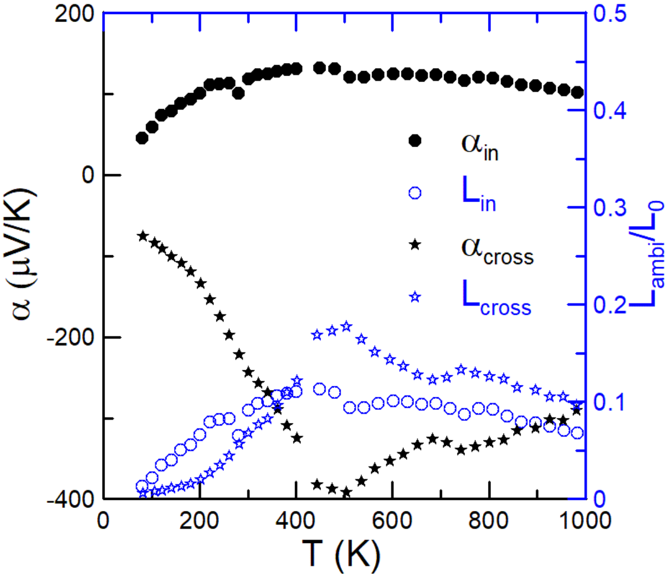

Figure S3 Thermopower and ambipolar Lorenz number ratio of Re_4Si_7 (crystal 1). In-plane thermopower (α_{in}) and cross-plane thermopower (α_{cross}) (solid black circles and stars, respectively). In-plane ratio of ambipolar Lorenz number to L_0 (2.44 x 10^{-8} WΩK^{-2}) and cross-plane ratio of ambipolar Lorenz number to L_0 (empty blue circles and stars, respectively).

At temperatures below 400 K, the ambipolar Lorenz number increase with temperature up to 20% and then decrease to about 10% at ~1000 K. From this quick estimation, the ambipolar term is not dominating the thermal conductivity.

Though it is a rough estimation, we can confirm that the holes in the cross-plane direction are extremely immobile which leads to electrons dominating the transport in that direction. Therefore, the transport is like a single carrier case and the ambipolar conductivity is a small portion.

The total thermal conductivity in the manuscript has been calculated assuming lattice contribution is constant at high temperature while ignoring an ambipolar contribution. However, this clearly overestimates the lattice contribution at high temperature to ultimately give a lower bounds on the anisotropic zT values.

Next, we will reevaluate the lattice thermal conductivity and extrapolate the total thermal conductivity to high temperature including the ambipolar term. First, we subtract the electronic contribution from our experimental data and fit the lattice contribution with a power function, shown below.

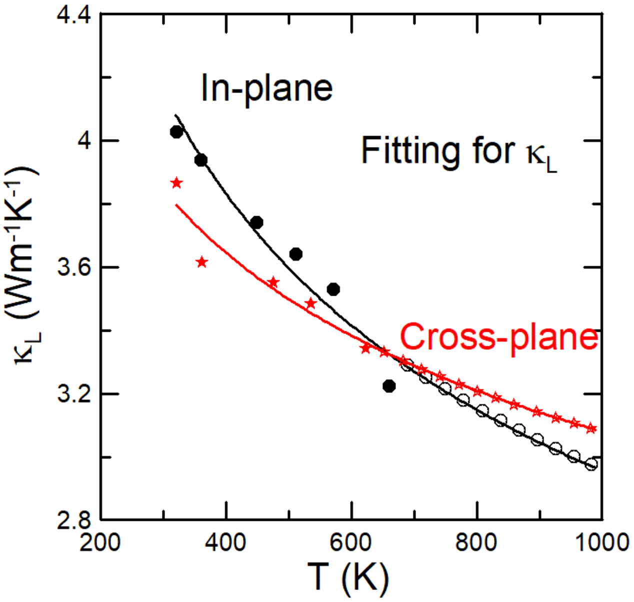

Figure S4 Lattice thermal conductivity Re_4Si_7 (crystal 1). In-plane lattice thermal conductivity (filled black circles) and cross-plane lattice thermal conductivity (filled red stars) each fit with a power function, respectively. Values derived from total thermal conductivity through by subtracting electronic contribution from experimental data using W-F law.

Finally, we extrapolate the total thermal conductivity with this lattice extrapolation and the new electronic/ambipolar contribution, shown below.

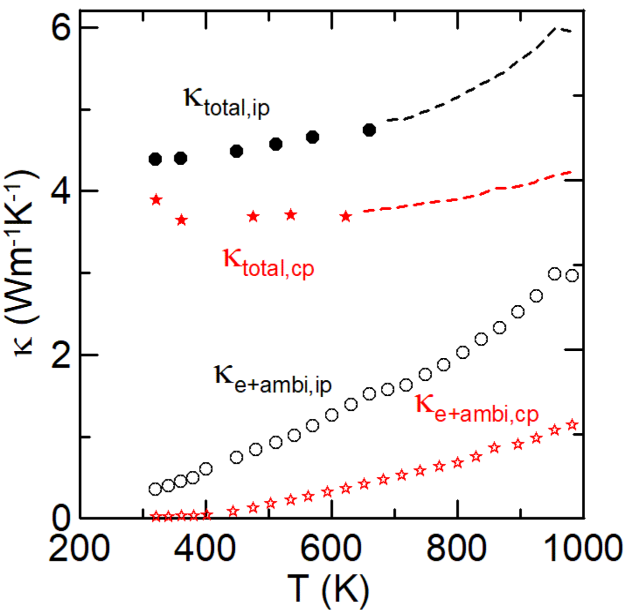

Figure S5 Thermal conductivity adjusted for ambipolar electronic contribution. In-plane electronic component of thermal conductivity plus ambipolar contribution ($\kappa_{e+ambi,ip}$) and cross-plane electronic component of thermal conductivity plus ambipolar contribution ($\kappa_{e+ambi,cp}$) (empty black circles and empty red stars, respectively). In-plane total thermal conductivity adjusted for ambipolar contribution ($\kappa_{total,ip}$) and cross-plane total thermal conductivity adjusted for ambipolar contribution ($\kappa_{total,cp)}$) (filled black circles and filled red stars, respectively).

Despite including the ambipolar term, these extrapolated thermal conductivity tensors are on average lower than those reported in the main text mainly due to the reduction of the lattice component to thermal conductivity at high temperature. Thus, the ambipolar thermal conductivity does not significantly contribute to the total thermal conductivity.

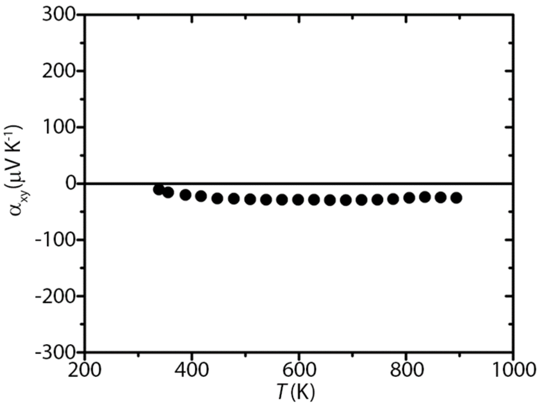

Figure S6: **Re_4Si_7 α_{xy} control measurement**. Experimental transverse thermopower with heat passed along in-plane direction, transverse voltage measured along cross-plane direction.

Supplement S5: Efficiency of Re_4Si_7 Transverse Thermoelectric Generator Device

The output power of the generator device is dictated by the transverse thermoelectric voltage (V_{xy}) and sample resistance (R) which were measure separately along the orientation shown in Figure 3c, and is determined by:

$$P_{out} = \frac{V_{xy}^2}{R} \tag{S5.1}$$

The device efficiency (η) then relates output power to heat input into the sample (Q_s) from the polyimide resistance heater:

$$\eta = \frac{P_{out}}{Q_S} \tag{S5.2}$$

The normalized device efficiency (η_N) as a fraction of Carnot ($\eta_C = 1 - T_C/T_H$) then becomes:

$$\eta_N = \frac{P_{out}}{Q_S \cdot \eta_C} \tag{S5.3}$$

A piece of quartz shaped to the dimensions of the Re_4Si_7 sample was used to quantify the degree of heat loss (Q_L) from the resistance heater (Q_{in}) into our generator device using the same ΔT that was used in the device ($\kappa_Q << \kappa_{Re4Si7}$). Quartz is an excellent standard for estimating the amount of heat loss from the source into the sample, since it has a well-known, low thermal conductivity (1.67 W m^{-1} K^{-1} at 560 K).[12] The amount of heat conducted through the quartz glass (Q_G) is accounted for by measuring the temperature gradient using the known thermal conductivity of quartz at ($Q_G = \kappa_Q \bullet \Delta T$). The heat losses are then determined by:

$$Q_L = Q_{in} - Q_G \tag{S5.4}$$

The net heat that is passed through the device (Q_D) can now be determined by:

$$Q_D = Q_S - Q_L \tag{S5.5}$$

The device efficiency (η) after factoring in heat losses from the sample then becomes:

$$\eta = \frac{P_{out}}{Q_D} \tag{S5.6}$$

The normalized device efficiency as a fraction of Carnot is then:

$$\eta_N = \frac{\eta}{\eta_C} \tag{S5.7}$$

Finally, the device transverse figure of merit, $Z_{xy}T$, corresponding to these measured device efficiencies can be extracted. For a resistive load matched to sample resistance, the device efficiency, η, is:

$$\eta = \frac{T_H - T_C}{T_H} \cdot \frac{\sqrt{1+Z_{xy}T}-1}{\sqrt{1-Z_{xy}T}+\frac{T_H}{T_C}} \tag{S5.8}$$

The corresponding device $Z_{xy}T$ can then be solved:

$$Z_{xy}T\ (\eta, T_H, T_C) = \eta \cdot T_H \cdot \frac{(-T_C^2 \cdot \eta \cdot T_H - 2 \cdot T_C^3 + \eta \cdot T_H^3 + 2T_H^2 \cdot T_C)}{T_C^2 \cdot (\eta \cdot T_H - T_H + T_C)^2} \qquad \text{S5.9}$$

The in-plane and cross-plane $\boldsymbol{\alpha}_{IP}$ and $\boldsymbol{\alpha}_{CP}$ were measured using isothermal conditions, which were then used to calculate $\boldsymbol{\alpha}_{xy}$. However, both our transverse $\boldsymbol{\alpha}_{xy}$ measurement for determining $z_{xy}T$ setup, as well as our device measurement setup $Z_{xy}T$, correspond to measurement configurations that are midway between adiabatic and isothermal due to the shape of the brass heat spreaders above and below the sample. We show in Figure 3d that the respective material ($z_{xy}T$) and device ($Z_{xy}T$) figures of merit are in excellent agreement, confirming the absence of losses in efficiency that are prevalent in longitudinal thermoelectric devices.

Supplement S6: Axis-dependent thermopower polarity in semiconductors

The anisotropic conduction polarity in near-intrinsic Re_4Si_7 has been previously attributed to a multi-carrier mechanism, in which conduction and valence band carriers have a large difference in mobility.[11, 13, 14] The mechanism also requires that either the electron or the hole mobilities, or both are very anisotropic. In this section, we illustrate how this generates large anisotropic Seebeck coeffcients using a simplified model for possible configurations of conduction and valence bands in semiconductors.

Consider the case of a nearly intrinsic semiconductor, at a temperature sufficient to thermally excite both electrons and holes. The electrons have a concentration n_e,

$$n_e = \int_{E_C}^{\infty} g_e(E) f_{FD}(E) dE \tag{S6.1}$$

where f_{FD} is the Fermi-Dirac distribution,

$$f_{FD}(E) = \frac{1}{1+\exp\left[(E-E_F)/(k_B T)\right]} \tag{S6.2}$$

and $g_e(E)$ is the density of states. Assuming that the electrons and holes fill bands with parabolic dispersion, and using the effective electron mass:

$$g_e(E) = \frac{8\pi\sqrt{2}}{h^3} m_e^{3/2} \sqrt{E - E_C} \tag{S6.3}$$

where the electron effective mass tensor can be calculated from the curvature of the conduction band at its minimum,

$$(m_e)_{ij}^{-1} = \frac{1}{\hbar^2} \frac{\partial^2 E}{\partial k_i \partial k_j}\bigg|_{E=E_C} \tag{S6.4}$$

The electron and hole mobilities are tensors, expressed in the in-plane/cross-plane (*IP*/*CP*) axes system as,

$$\overleftrightarrow{\mu}_e = \begin{bmatrix} \mu_{e,IP} & 0 \\ 0 & \mu_{e,CP} \end{bmatrix}, \overleftrightarrow{\mu}_h = \begin{bmatrix} \mu_{h,IP} & 0 \\ 0 & \mu_{h,CP} \end{bmatrix} \tag{S6.5}$$

whose *IP* and *CP* components are given by

$$\mu = \frac{e\tau}{m_e} \tag{S6.6}$$

and so on for the other components of indices *CP* and m_h. We approximate the energy dependence of the average scattering time by the standard expression

$$\tau(E) = \tau_0 E^{-\lambda} \tag{S6.7}$$

with $\lambda = -1/2$, assuming acoustic phonons as the dominant scatterers. The partial electron conductivities are then also tensors:

$$\overleftrightarrow{\sigma}_e \approx n_e e \overleftrightarrow{\mu}_e, \quad \overleftrightarrow{\sigma}_h \approx n_h e \overleftrightarrow{\mu}_h \tag{S6.8}$$

We further assume that the partial thermopowers of electrons and holes, α_e and α_h, are scalars, because they are directly related to the entropy of the quasi-particles divided by their charge. We cthen compute $\overleftrightarrow{\sigma}_e, \overleftrightarrow{\sigma}_h$, α_e, α_h from transport integrals.[15]

The total thermopower is given by the conductivity-weighted average of the partial thermopowers, as in (Eq S3.1), except that here the thermopower is a tensor:

$$\overleftrightarrow{\alpha} = (\alpha_e \overleftrightarrow{\sigma}_e + \alpha_h \overleftrightarrow{\sigma}_h)(\overleftrightarrow{\sigma}_e + \overleftrightarrow{\sigma}_h)^{-1} \tag{S6.9}$$

This can be worked out separately for the *IP* and *CP* directions to give:

$$\alpha_{IP} = \frac{\alpha_e + \frac{n_h \mu_{h,IP}}{n_e \mu_{e,IP}} \alpha_h}{1 + \frac{n_h \mu_{h,IP}}{n_e \mu_{e,IP}}} \;;\quad \alpha_{CP} = \frac{\alpha_e + \frac{n_h \mu_{h,CP}}{n_e \mu_{e,CP}} \alpha_h}{1 + \frac{n_h \mu_{h,CP}}{n_e \mu_{e,CP}}} \tag{S6.10}$$

Equation (6.10) contains all the ingredients necessary to understand the axis-dependent conduction polarity behavior that shows up at specific doping levels of the semiconductor (Fig. S7).

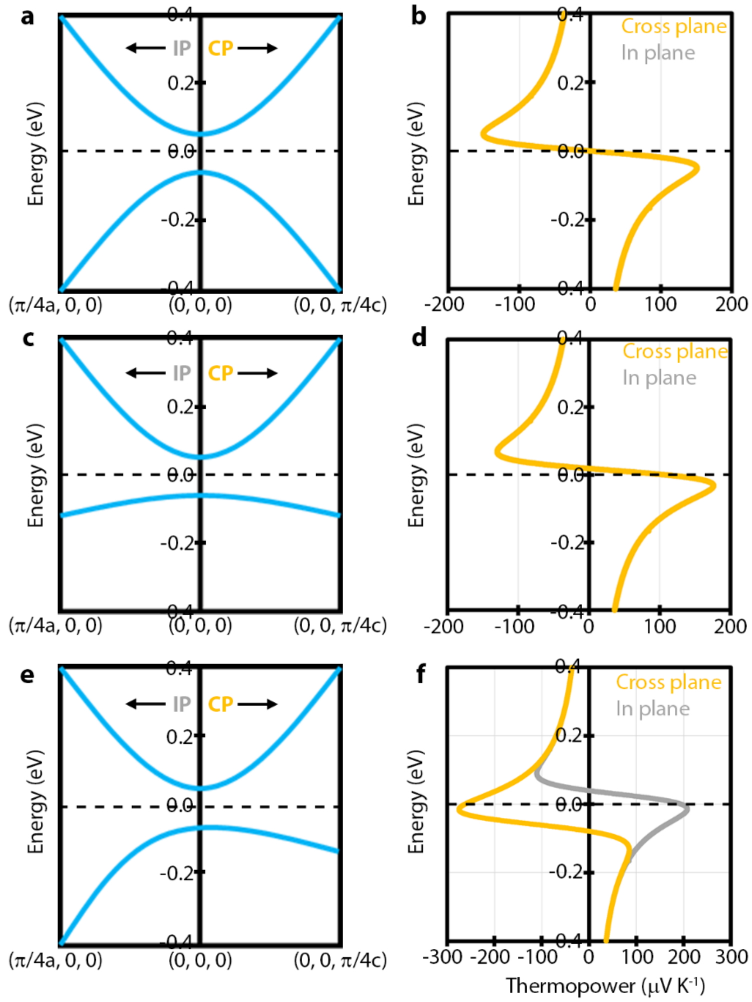

Figure S7 Illustration of the multi-carrier mechanism. a, Band diagram of a E_g= 0.12 eV gapped material having an isotropic conduction and valence band, with $m_e = |m_h| = 0.2\ m_0$. **b,** The predicted in-plane and cross-plane 300 K thermopowers at different E_F for the band structure shown in **a.** **c,** Band diagram and **d,** E_F dependent 300 K thermopowers for a E_g = 0.12 eV gapped material having an isotropic conduction and valence band with $m_e = 0.2\ m_0$ and $m_h = 1.0\ m_0$. **e,** Band diagram and **f,** E_F dependent 300 K thermopowers for the anisotropic Re_4Si_7-like material having a E_g= 0.12 eV gap, a relatively isotropic conduction band with $m_{e,CP} = 0.26\ m_0$, $m_{e,IP} = 0.49\ m_0$ and an anisotropic hole pocket with $|m_{h,CP}| = 7.7\ m_0$ and $|m_{h,IP}| = 0.1\ m_0$.

For all materials, in plane corresponds to the (*h*00) direction, cross plane corresponds to the (00*l*) direction. In the frames a, c and e of Fig. S7, we plot toy model band diagrams of a simple layered 0.12 eV gap semiconductor with a single conduction and valence band. Here, in-plane corresponds to the (*h*00) directions with isotropic properties in the plane, while cross-plane corresponds to the (00*l*) direction and E_F = 0 is set at the mid-gap. In frames b, d and f, we calculate the *IP* and *CP* thermopowers for these semiconductors at 300 K as a function of the position of the chemical potential on the *y*-axis. The *y*-axes of frame a and b are identical, as with c and d, and e and f. In other words, frames b, d and f represent the values of the *IP* (yellow) and *CP* (grey) thermopowers, as a function of chemical potential and thus doping level.

In frames a and b, we consider the case of an isotropic semiconductor (i.e. $\mu_{IP}=\mu_{CP}$) with symmetric conduction and valence bands where $m_e = |m_h| = 0.2\ m_0$. The *IP* and *CP* thermopowers are the same at all chemical potentials. With the chemical potential in the conduction band, the thermopower is negative. Its absolute value increases as it approaches the band edge, because in metals and degenerate semiconductors, the partial thermopower $\alpha_e \propto 1/E_F$, where E_F is the Fermi level measured from the band edge. As long as the chemical potential is high in the conduction band, there are few holes so the term $\frac{n_h\mu_h}{n_e\mu_e} \to 0$ in equation S6.10. When the chemical potential enters the gap, n_h starts increasing, and so does the $\frac{n_h\mu_h}{n_e\mu_e}\alpha_h$term, limiting any further increase in $|\alpha|$. When the chemical potential is at mid-gap, $\frac{n_h\mu_h}{n_e\mu_e} = 1$ and because the bands are symmetric, $\alpha_e = -\alpha_h$ giving $\alpha = 0$. As the chemical potential further nears the valence band edge, and then enters it, the process above repeats, with the signs reversed. Consequently, the curve of thermopower versus chemical potential is perfectly antisymmetric, as shown in Fig. S7b.

In frames c and d, we consider the case of an isotropic semiconductor (i.e. $\mu_{IP}=\mu_{CP}$) with the conduction band having a lower effective mass ($m_e = 0.2\ m_0$) than the valence bands ($|m_h| = 1.0\ m_0$), and thus $\mu_e > \mu_h$. The process above repeats, because when $\frac{\mu_h}{\mu_e} < 1$ the term $\frac{n_h\mu_h}{n_e\mu_e} \neq 1$ when the chemical potential is at mid-gap. As a result, the point where $\alpha=0$ is shifted toward the conduction band. The curve of α as function of the chemical potential is no longer antisymmetric. At the same time, the maximum *n*-type thermopower has a smaller absolute value than the maximum *p*-type thermopower. Again, the *IP* and *CP* thermopowers are identical at all chemical potentials.

In frames e and f, we now consider the case of an anisotropic semiconductor with the bands having similar effective masses to Re_4Si_7. Here, we assume a relatively isotropic conduction band with $m_{e,CP} = 0.26\ m_0$, $m_{e,IP} = 0.49\ m_0$. Along the *IP* direction, the valence band has a similar effective mass $|m_{h,IP}| = 0.1\ m_0$ to the conduction band. Along the *CP* direction, the valence band has a much larger effective mass $|m_{h,CP}| = 7.7\ m_0$ than the conduction band. Therefore, $\mu_{e,IP} \cong \mu_{e,CP} \cong \mu_{h,IP} > \mu_{h,CP}$, which affects the balancing of electron and hole contributions differently for α_{IP} and α_{CP} in (Eq. S6.10). In particular, since $\mu_{h,CP}/\mu_{e,CP} > 30$, α_{CP} becomes dominated by α_e, and thus will be much more negative than α_{IP} close to the band edges. Additionally, as the density of states is determined by the full mass tensor, the evolution of n_h and n_e with chemical potential will be different in frame f, compared to frame b and d. Overall, both of these effects combine to cause α_{CP} to shift down in energy, and flip from negative to positive sign at chemical potentials close to the valence band, whereas α_{IP} will change sign when the chemical potential is slightly above mid gap. As a result, there exists a range of chemical potentials (from $E-E_F = -0.08$ to $+0.04$ eV in Fig. S7f) where simultaneously $\alpha_{IP}>0$ and $\alpha_{CP}<0$.

Again, Fig. S7f represents schematically a simplified two-band, band structure with effective masses close to those in Re_4Si_7. Remarkably, this analytical model predicts values of the thermopower that are in close agreement with the values measured for crystal 1. Specifically, at 0.02 eV above midgap, the predicted 300 K α_{IP} is +120 μV K^{-1} and α_{CP} is -230 μV K^{-1}, which is nearly identical to our measured α_{IP} of 119 μV K^{-1} and α_{CP} of -243 μV K^{-1}. Finally, this model indicates that in a narrow gap semiconductor that has a highly anisotropic valence band, and an isotropic conduction band, axis-dependent conduction polarity will maximize at chemical potentials close to the valence band.

Supplement S7. DFT calculations supporting Si vacancies as p-type dopants.

DFT calculations were performed to evaluate the behavior of Si vacancies as dopants in Re_4Si_7. Indeed these calculations show that Si vacancies in Re_4Si_7 act as *p*-type dopants. Figure S7 shows the calculated energy dependent density of states (DOS) for a 352 atom Re_4Si_7 super cell ($Re_{128}Si_{224}$) along with the density of states for the same supercell with a single neutral silicon vacancy ($Re_{128}Si_{223}$). In both cases, 0 eV corresponds to the valence band maximum. The red dashed line is the calculated Fermi level for the unit cell with Si vacancies. Since this Fermi level cuts through the valence band, it shows that the Si vacancies act as *p*-type dopants.

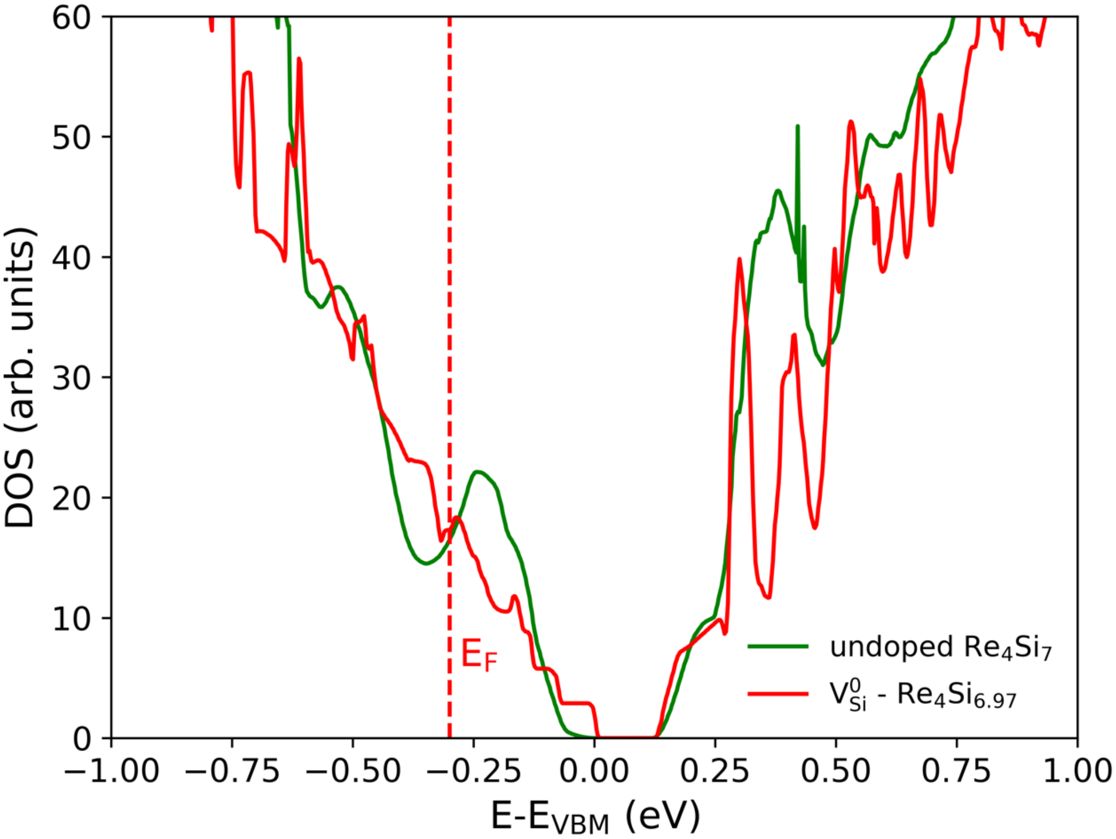

Figure S8: **DOS for stoichiometric and Si-deficient Re_4Si_7**. Calculated DOS for a supercell of Re_4Si_7 containing a stoichiometric $Re_{128}Si_{224}$ ratio (green) and Si-deficient $Re_{128}Si_{223}$ ratio (red). In both plots 0 eV corresponds to the valence band maximum. The Fermi level for the Si-deficient compound is depicted at the dashed line.

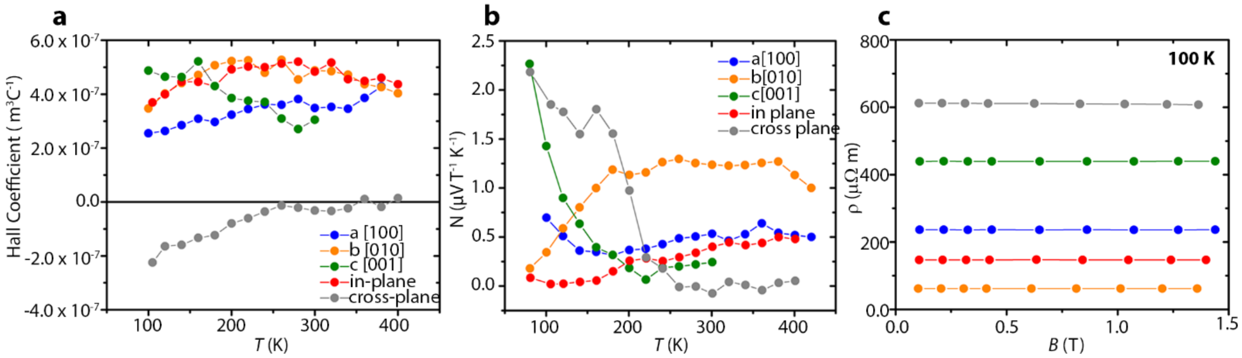

Figure S9: **Hall, Nernst, Magnetoresistance for near-intrinsic Re_4Si_7 crystal 1**. **a**, Temperature-dependent Hall coefficient. **b**, Temperature-dependent Nernst thermopower. **c**, Field-dependent electrical resistivity showing little to no magnetoresistance.

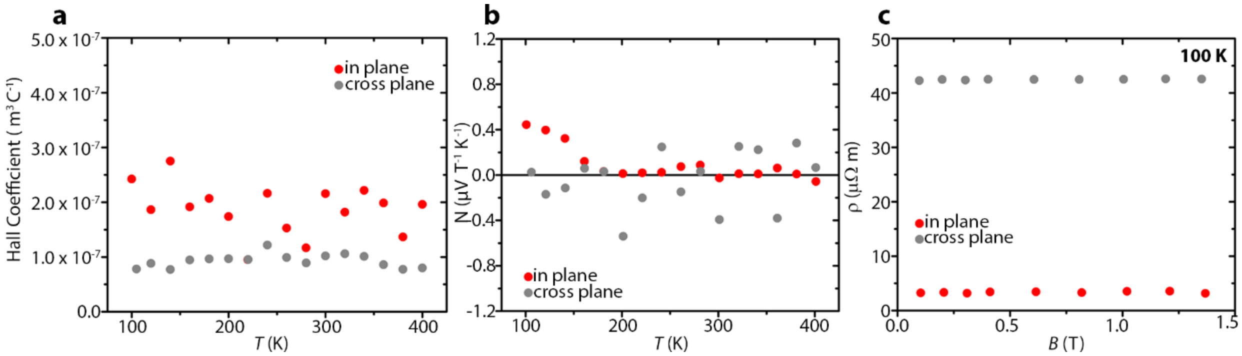

Figure S10: **Hall, Nernst, Magnetoresistance for Re_4Si_7 crystal 3**. **a**, Temperature-dependent Hall coefficient. **b**, Temperature-dependent Nernst thermopower. **c**, Field-dependent electrical resistivity showing little to no magnetoresistance.

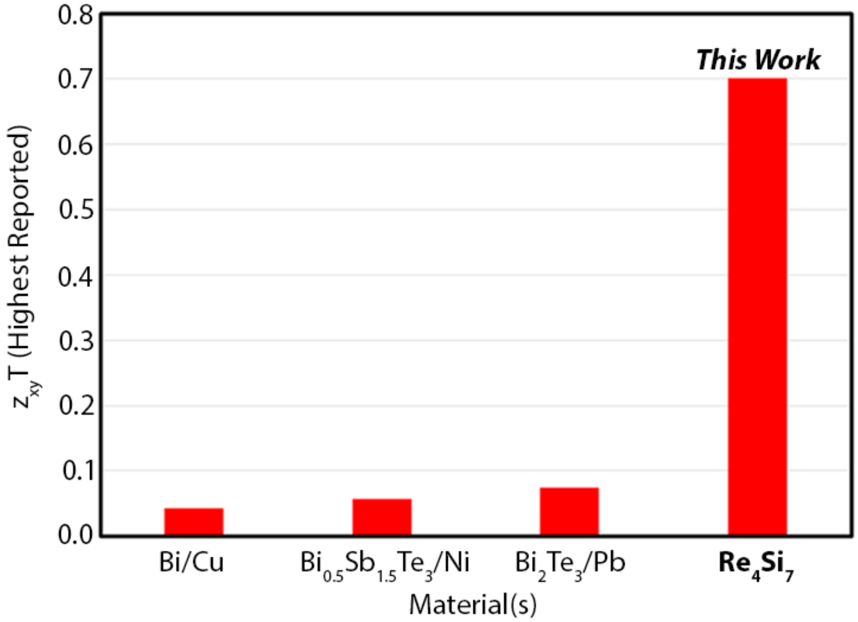

Figure S11: **Comparison of reported $z_{xy}T$ values in other material systems Re_4Si_7.** Bi/Cu, $z_{xy}T=0.042$(predicted)[16]; $Bi_{0.5}Sb_{1.5}Te_3$/Ni, $z_{xy}T=0.057$[17]; Bi_2Te_3/Pb, $z_{xy}T=0.074$[18]; Re_4Si_7 (this work), $z_{xy}T=0.7 \pm 0.15$

,

Supplemental References

1. R. R. Heikes and R. W. Ure, *Thermoelectricity: science and engineering*, Interscience Publishers, New York, 1961.
2. J. P. Heremans, *Tetradymites: Bi_2Te_3-Related Materials*, CRC Press, Boca Raton, 2017.
3. H. J. Goldsmith, *Introduction to Thermoelectricity*, Springer, Berlin, 2010.
4. C. Zhou, S. Birner, Y. Tang, K. Heinselman and M. Grayson, *Phys. Rev. Lett.*, 2013, **110**, 227701.
5. T. H. Geballe and G. W. Hull, *Phys. Rev.*, 1954, **94**, 1134-1140.
6. T. H. Geballe and G. W. Hull, *Phys. Rev.*, 1955, **98**, 940-947.
7. J. P. Heremans, V. Jovovic, E. S. Toberer, A. Saramat, K. Kurosaki, A. Charoenphakdee, S. Yamanaka and G. J. Snyder, *Science*, 2008, **321**, 554-557.
8. J. P. Heremans, R. J. Cava and N. Samarth, *Nat. Rev. Mater.*, 2017, **2**, 17049.
9. B. Lenoir, A. Dauscher, M. Cassart, Y. I. Ravich and H. Scherrer, *J. Phys. Chem. Solids*, 1998, **59**, 129-134.
10. H. Muta, T. Kanemitsu, K. Kurosaki and Y. Shinsuke, *Material Transactions*, 2006, **47**, 1453-1457.
11. J. J. Gu, M. W. Oh, H. Inui and D. Zhang, *Phys. Rev. B: Condens. Matter Mater. Phys.*, 2005, **71**, 4-7.
12. O. A. Sergeev, A. G. Shashkov and A. S. Umanskii, *Journal of Engineering Physics*, 1982, **43**, 1375-1383.
13. M.-W. Oh, J.-J. Gu, H. Inui, M.-H. Oh and D.-M. Wee, *Phys. B*, 2007, **389**, 367-371.
14. A. B. Filonov, A. E. Krivosheev, L. I. Ivanenko, G. Behr, J. Schumann, D. Souptel and V. E. Borisenko, *Semiconductors*, 2005, **39**, 395-399.
15. E. H. Putley, *The Hall Effect and Semiconductor Physics*, Dover Publications Inc., New York, 1987.
16. T. Kanno, S. Yotsuhashi, A. Sakai, K. Takahashi and H. Adachi, *Appl. Phys. Lett.*, 2009, **94**, 1-3.
17. K. Takahashi, T. Kanno, A. Sakai, H. Tamaki, H. Kusada and Y. Yamada, *Sci. Rep.*, 2013, **3**, 1-3.
18. C. Reitmaier, F. Walther and H. Lengfellner, *Appl. Phys. A.*, 2011, **105**, 347-349.